

21 Scattering and partial wave analysis

In this chapter we deal with elastic two-body scattering between two particles with masses m_1 and m_2 . We shall first assume that the two particles are spinless and that particle 1 scatters in the potential $V(r)$ of particle 2 (figure 21.1). At distances of separation larger than the range R of the potential the projectile can be described by a plane wave moving along the z -axis, which is then scattered in the spherically symmetrical potential $V(r)$.

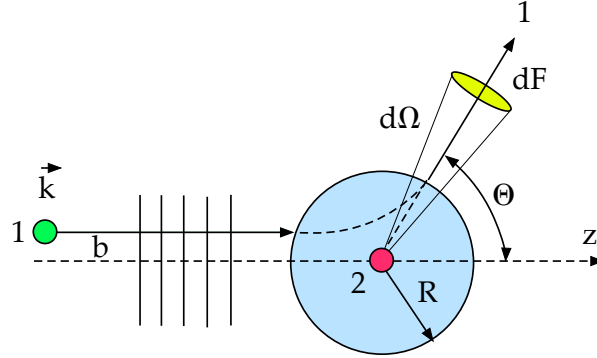


Figure 21.1: Elastic scattering $1 + 2 \rightarrow 1 + 2$ by a potential of range R .

At large distances ($r > R$) from the scattering center the scattered particle 1 is represented by a spherical wave emitted from the origin at $r = 0$. The wave function is given by

$$\psi(r, \theta) = e^{ikz} + f(\theta) \frac{e^{ikr}}{r}, \quad (21.1)$$

up to an overall normalization constant, and where k is the momentum of both incident and scattered particles, that is the momentum expressed in the center-of-mass system. The function $f(\theta)$ is the **scattering amplitude**. Using (8.13) one obtains from the total energy E_1 and momentum p_1 in the laboratory

$$k = \beta\gamma E_1 - \gamma p_1 = \beta\gamma m_2, \quad (21.2)$$

hence the velocity of the center of mass,

$$\beta = \frac{p_1}{E_1 + m_2}. \quad (21.3)$$

The relativistic γ -factor is

$$\gamma = \frac{1}{\sqrt{1 - \frac{p_1^2}{(E_1 + m_2)^2}}} = \frac{E_1 + m_2}{\sqrt{m_1^2 + m_2^2 + 2E_1 m_2}}, \quad (21.4)$$

and therefore from (21.2)

$$k = \frac{m_2 p_1}{\sqrt{m_1^2 + m_2^2 + 2E_1 m_2}} \simeq \frac{m_2 p_1}{m_1 + m_2} = \mu \beta_1 \quad (21.5)$$

in the non-relativistic limit $E_1 \simeq m_1$, where β_1 is the incident velocity in the laboratory and $\mu = \frac{m_1 m_2}{m_1 + m_2}$ the reduced mass. For very heavy targets $m_2 \gg m_1$ one obtains the incident momentum in the laboratory, $k = m_1 \beta_1$.

Let us relate the scattering amplitude $f(\theta)$ in (21.1) to the differential cross section $\frac{d\sigma}{d\Omega}$. We shall derive a parametrization of $f(\theta)$ in terms of **partial waves**, that is as a function of angular momentum contributions. We have seen that the angular momentum is related to the momentum and to the impact parameter through $|\vec{L}| = \sqrt{\ell(\ell+1)} = bk$ (see equation 1.1). The maximum value of the quantum number ℓ contributing to the scattered wave is therefore $\ell_{\max} \simeq Rk$. The goal is therefore to find an expansion for $f(\theta)$ in terms of ℓ which can be truncated at small values of ℓ , depending on the magnitudes of R and k .

The incoming flux through the surface $d\sigma = 2\pi b db$ is equal to the outgoing flux through the surface dF (figure 21.1, see also figure 1.4). Hence in the center-of-mass frame

$$\beta_1^* |e^{ikz}|^2 d\sigma = \beta_1^* |f(\theta)|^2 \left| \frac{e^{ikr}}{r} \right|^2 dF, \quad (21.6)$$

where β_1^* is the velocity in the center of mass and $dF = r^2 d\Omega$. The differential cross section in the center-of-mass frame is then given by

$$\boxed{\frac{d\sigma}{d\Omega} = |f(\theta)|^2}. \quad (21.7)$$

For $V(r) = 0$ the wave function is the incoming plane wave for which we use the expansion (13.28) into spherical Bessel functions $j_\ell(kr)$, which can be approximated by

$$j_\ell(kr) \rightarrow \frac{\sin(kr - \ell\frac{\pi}{2})}{kr} \quad (21.8)$$

at sufficiently large distances from the scattering center so that $kr \gg \ell$. Therefore

$$\begin{aligned} e^{ikz} &= \sum_{\ell=0}^{\infty} (2\ell+1) i^\ell \left[\frac{e^{i(kr - \ell\frac{\pi}{2})} - e^{-i(kr - \ell\frac{\pi}{2})}}{2ikr} \right] P_\ell(\cos\theta) \\ &\equiv \frac{1}{r} \sum_{\ell=0}^{\infty} A_\ell [e^{i(kr - \ell\frac{\pi}{2})} - e^{-i(kr - \ell\frac{\pi}{2})}] \quad \text{with } A_\ell \equiv \frac{(2\ell+1)i^\ell}{2ik}. \end{aligned} \quad (21.9)$$

We have expressed the plane wave as a sum of incoming spherical waves (second terms in the brackets with $z = -r$) and outgoing spherical waves (first terms). Switching on the potential $V(r)$ now modifies the contribution from the outgoing spherical wave. Since the incident momentum k is equal to the outgoing momentum, the wavelength of the oscillation does not change and we take this contribution into account by multiplying the amplitude of each outgoing partial waves in (21.9) by a complex number that is usually written as $e^{2i\delta_\ell}$, where the real **phase shifts** δ_ℓ depend only on k . In the presence of absorption (e.g. excitation) or inelasticities (such as the production of other particles in the final state) the amplitudes of the outgoing waves for the reaction $1 + 2 \rightarrow 1 + 2$ are reduced by a factor $\eta_\ell(k) < 1$. For purely elastic two-body scattering $\eta_\ell = 1$. The wave function (21.1) reads

$$\psi = \frac{1}{r} \sum_{\ell=0}^{\infty} A_\ell [e^{i(kr - \ell\frac{\pi}{2})} \eta_\ell e^{2i\delta_\ell} - e^{-i(kr - \ell\frac{\pi}{2})}]. \quad (21.10)$$

The scattering amplitude is obtained by subtracting from ψ the incoming wave (21.9). With $e^{-i\ell\frac{\pi}{2}} = (-i)^\ell$ one obtains

$$f(\theta) = re^{-ikr}(\psi - e^{ikz}) = \sum_{\ell=0}^{\infty} A_\ell (-i)^\ell (\eta_\ell e^{2i\delta_\ell} - 1). \quad (21.11)$$

Hence

$$f(\theta) = \frac{1}{k} \sum_{\ell=0}^{\infty} (2\ell + 1) \left[\frac{\eta_\ell e^{2i\delta_\ell} - 1}{2i} \right] P_\ell(\cos \theta) \quad (21.12)$$

is the **elastic scattering** amplitude. Since the series (21.12) can be truncated at $\ell_{\max} = kR$, only few parameters are needed to describe the differential elastic cross section (21.7) at low energy. This parametrization of the interaction is only useful as long as the number of partial waves is not too large, that is for momenta below a few hundred MeV/c. We shall deal with the phase shifts δ_ℓ in more detail below.

The total **elastic** cross section for the reaction $1 + 2 \rightarrow 1 + 2$ is given by

$$\begin{aligned} \sigma_e &= \int |f(\theta)|^2 d\Omega = \frac{2\pi}{k^2} \sum_{\ell=0}^{\ell_{\max}} (2\ell + 1)^2 |f_\ell(k)|^2 \overbrace{\int_{-1}^{+1} P_\ell^2(\cos \theta) d\cos \theta}^{\frac{2}{2\ell+1}} \\ &= \frac{4\pi}{k^2} \sum_{\ell=0}^{\ell_{\max}} (2\ell + 1) |f_\ell(k)|^2 \end{aligned} \quad (21.13)$$

$$= \frac{\pi}{k^2} \sum_{\ell=0}^{\ell_{\max}} (2\ell + 1) |\eta_\ell e^{2i\delta_\ell} - 1|^2, \quad (21.14)$$

where we have defined the partial wave amplitude

$$f_\ell(k) \equiv \frac{\eta_\ell(k) e^{2i\delta_\ell(k)} - 1}{2i}. \quad (21.15)$$

The cross section σ_r for inelastic scattering is determined by the intensity $(1 - \eta_\ell)^2$. From (21.14) one guesses that

$$\sigma_r = \frac{\pi}{k^2} \sum_{\ell=0}^{\ell_{\max}} (2\ell + 1) (1 - \eta_\ell^2) \quad (21.16)$$

(for details see [1] p. 122). Let us also compute with (21.14) and (21.16) the total cross section σ_t for the reaction $1 + 2$:

$$\begin{aligned} \sigma_t = \sigma_e + \sigma_r &= \frac{\pi}{k^2} \sum_{\ell=0}^{\ell_{\max}} (2\ell + 1) [(\eta_\ell^2 - 2\eta_\ell \cos 2\delta_\ell + 1) + (1 - \eta_\ell^2)] \\ &= \frac{2\pi}{k^2} \sum_{\ell=0}^{\ell_{\max}} (2\ell + 1) (1 - \eta_\ell \cos 2\delta_\ell). \end{aligned} \quad (21.17)$$

On the other hand from (21.12) the imaginary part of $f(\theta)$ at $\theta = 0$ is

$$\text{Im}f(0) = \frac{1}{2k} \sum_{\ell=0}^{\ell_{\max}} (2\ell + 1)(1 - \eta_{\ell} \cos 2\delta_{\ell}). \quad (21.18)$$

This leads to the important **optical theorem**

$$\boxed{\sigma_t = \frac{4\pi}{k} \text{Im}f(0)} \quad (21.19)$$

which relates the **total** cross section for $1 + 2$ to the forward scattering amplitude for elastic scattering $1 + 2 \rightarrow 1 + 2$.

21.1 Low energy elastic scattering

What is the physical meaning of the phase shift δ_{ℓ} which enters the wave function (21)? Let us consider a spherically symmetric potential $V(r)$. The radial part $u(r) = r\psi$ of the wave function satisfies the radial Schrödinger equation

$$\frac{d^2u}{dr^2} + \left[k^2 - 2\mu V(r) - \frac{\ell(\ell + 1)}{r^2} \right] u = 0, \quad (21.20)$$

where the energy of the incident particle is $k^2/2\mu$. We restrict ourselves to **very low energy** elastic scattering for which only $\ell = 0$ contributes and abbreviate $\delta_0 \equiv \delta$ (S -wave scattering). According to (21.9) and in the absence of potential the wave function $u(r)$ is proportional to $\sin kr$ at large distances, and is identical to the incident wave function. Indeed, $\sin kr$ is the solution of (21.20) with $V(r) = 0$, which is regular at the origin so that ψ remains finite at $r = 0$. When $V(r)$ is switched on the wave function becomes with (21.10) and $\eta_0 = 1$

$$u(r) \propto e^{i\delta} [e^{i\delta + ikr} - e^{-i\delta - ikr}] \propto \sin(kr + \delta) \quad (21.21)$$

at large distances r . One sees that for $\delta > 0$ the zeroes of the sine wave are shifted towards smaller values of r and thus $u(r)$ is **attracted** into the potential region. In contrast, for $\delta < 0$ the potential is **repulsive** and shifts $u(r)$ towards larger values of r . The same conclusions can be drawn for higher partial waves.

As a concrete example, consider low energy scattering by a square-well potential with radius R_0 , so that $V(r) \equiv -V_0 < 0$ for $r < R_0$ and $V(r) \equiv 0$ for $r > R_0$ (figure 21.2a). The internal wave function ($r < R_0$) satisfying (21.20) with $u_i(0) = 0$ is $u_i(r) = A \sin k_i r$, where

$$k_i^2 = k^2 + 2\mu V_0 > 0. \quad (21.22)$$

The function $u_i(r)$ can oscillate, as shown in figure 21.2b, depending on μ and V_0 . The external wave function $u(r)$ (for $r > R_0$) is given by (21.21) but the two functions must match at $r = R_0$. We normalize $u(r)$ so that $u(0) = 1$, hence write $u(r) \equiv \frac{\sin(kr + \delta)}{\sin \delta}$. Then the magnitude (and sign) of A is determined by the relation

$$A \sin k_i R_0 = \frac{\sin(kR_0 + \delta)}{\sin \delta}. \quad (21.23)$$

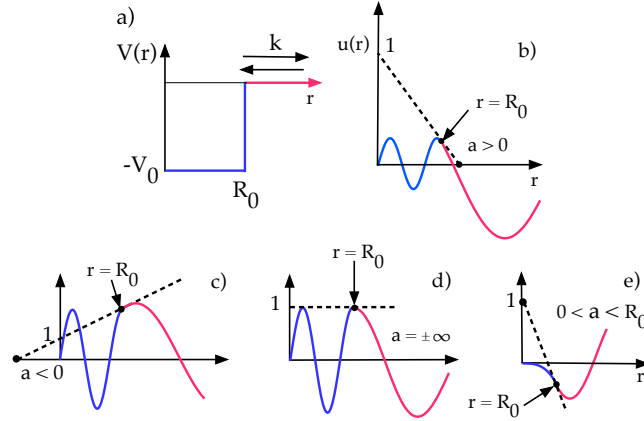


Figure 21.2: Low energy elastic scattering by a square potential (a). The blue curves in (b)–(e) show the internal waves $u_i(r)$ for $V(r) = -V_0$, the red curves the external waves $u(r)$. The dashed straight lines show the low energy approximation $v(r)$ to $u(r)$, extrapolated to $v(0) = 1$. The potential can be repulsive ($a > 0$, $\delta < 0$) as in (b), attractive ($a < 0$, $\delta > 0$) as in (c), or resonant as in (d); the curves in (e) correspond to a repulsive square potential $V(r) = +V_0$ (see the text).

For k small (long wavelength) the external wave function $u(r)$ becomes linear in r and can be written as $u(r) \rightarrow v(r) = 1 - \frac{r}{a}$. The constant a is the **scattering length**, the distance from the origin at which $v(r)$ vanishes. The matching conditions at the boundary $r = R_0$ are

$$A \sin k_i R_0 = \left(1 - \frac{R_0}{a}\right) \quad \text{and} \quad A k_i \cos k_i R_0 = -\frac{1}{a} \quad (21.24)$$

for the derivatives, hence

$$\frac{1}{k_i} \tan k_i R_0 = R_0 - a \quad (21.25)$$

or

$$a = R_0 \left[1 - \frac{\tan k_i R_0}{k_i R_0} \right]. \quad (21.26)$$

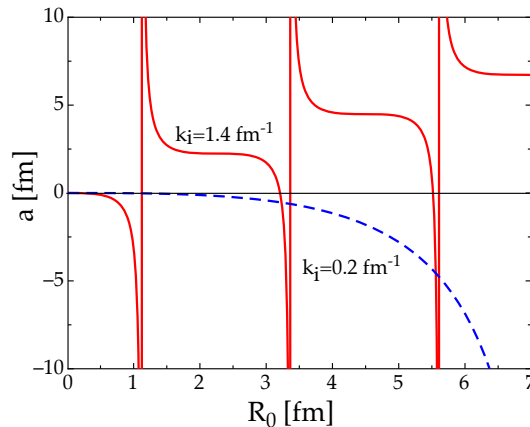


Figure 21.3: Scattering length a vs. potential range R_0 for small and large values of k_i (see the text).

Figure 21.3 shows how the scattering length a varies with the radius R_0 of the potential. For light particles and shallow potentials ($\sqrt{2\mu V_0} \lesssim 1/R_0$) the potential is attractive (blue dotted line), while for heavier projectiles in stronger nuclear potentials the function $u_i(r)$ can perform more than one oscillation (red curve). For example, for a low energy neutron scattered by a nuclear potential of depth $V_0 = 40$ MeV (see equation (3.23)) $k_i \simeq \sqrt{M_n V_0} = 274 \text{ MeV} = 1.4 \text{ fm}^{-1}$, corresponding to a de Broglie wavelength of $2\pi/k_i = 4.5 \text{ fm}$ which is smaller than the size of very heavy nuclei. Figure 21.3 shows that the scattering length can be positive or negative with a preference for the former, with consequences that will be discussed in more detail below (section 21.4).

The relation between scattering length and phase shift is obtained by constructing the straight line $v(r)$ tangent to the wave functions at $r = R_0$ (dashed lines in figure 21.2):

$$v(r) = 1 - \frac{r}{a} \simeq \frac{\sin(kr + \delta)}{\sin \delta} = \frac{\overbrace{\sin kr}^{\simeq kr} \cos \delta + \overbrace{\cos kr}^{\simeq 1} \sin \delta}{\sin \delta} \simeq kr \cot \delta + 1. \quad (21.27)$$

Therefore at very low momenta

$$\boxed{\tan \delta = -ak}. \quad (21.28)$$

For $k = 0$ the phase δ is equal to 0 or π . In the first case, as k increases δ becomes negative (repulsive potential) for positive a or positive (attractive potential) for negative a . However, for $\delta = \pi$ the **opposite** is true: as k increases $\tan \delta$ decreases from 0 to negative values and thus a is positive. This occurs for example in the 3S_1 wave of low energy np scattering (section 21.1.1) and is related to the existence of the deuteron bound state.

An example of attractive scattering is shown in figure 21.2c. **Resonance** occurs when a decreases towards $a = -\infty$ ($\delta = \frac{\pi}{2}$). The internal wave function then reaches its **maximum** amplitude $u_i(R_0) = u(R_0)$ (horizontal dashed line in figure 21.2d). Beyond $\delta = \frac{\pi}{2}$ the scattering length is positive, decreasing from $+\infty$. This corresponds to a square potential with $V(r) = +V_0 > 0$. For incoming energies $k^2/2\mu < V_0$ the force is repulsive: $k_i^2 = k^2 - 2\mu V_0 < 0$ and hence k_i is imaginary. Therefore $u_i(r)$ increases exponentially from $u(0) = 0$: $u_i(r) \propto \exp(|k|r)$ while $u(r) \propto \sin(kr + \delta)$ at large distances. Matching the two functions at $r = R_0$ then leads to the positive scattering length $a < R_0$ (repulsive potential with $\delta < 0$, figure 21.2e).

According to (21.14) the cross section for low energy purely elastic scattering is

$$\sigma_e = \frac{\pi}{k^2} |e^{2i\delta} - 1|^2 = \frac{4\pi}{k^2} \sin^2 \delta \simeq \frac{4\pi}{k^2} \tan^2 \delta = 4\pi a^2, \quad (21.29)$$

which is equal to the surface of a sphere of radius a . The scattering amplitude (21.12) is independent of θ (isotropic differential cross section in the center-of-mass system) and is equal to

$$f = \frac{1}{k} e^{i\delta} \sin \delta = \frac{1}{k} (\cos^2 \delta \tan \delta + i \sin^2 \delta), \quad (21.30)$$

hence with (21.28)

$$\boxed{\lim_{k \rightarrow 0} f(k) = -a}. \quad (21.31)$$

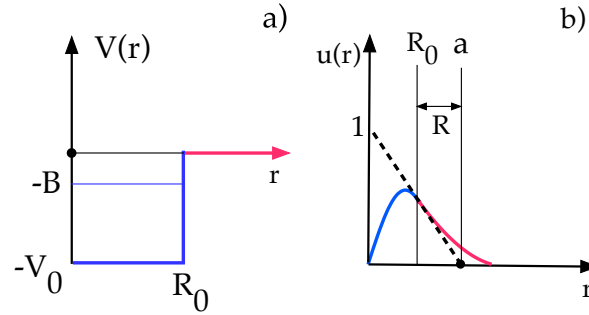


Figure 21.4: Potentials $V(r) = -V_0$ for $r < R_0$ (a) and corresponding wave functions for a bound state (b).

In the low energy limit the total wave function (21.1) is then simply given by

$$\psi(r) \propto 1 - \frac{a}{r} \quad (21.32)$$

at large distances from the scattering center.

21.1.1 Low energy neutron-proton scattering and the deuteron

Let us deal with a bound state in the square-well (figure 21.4a). The energy of the bound particle is its binding energy B , hence we replace k_i^2 in (21.22) by $k_i^2 = 2\mu[-B - V(r)] = 2\mu(V_0 - B) > 0$ and therefore $u_i(r) \propto \sin k_i r$. The energy of the external wave function is $-B$, hence $k^2 = -2\mu B$. Thus k becomes imaginary and $u(r) \propto \exp(-|k|r)$ with $|k| = \sqrt{2\mu B}$. The wave function decreases exponentially outside the well with decay constant $R = \frac{1}{\sqrt{2\mu B}}$. Matching the two functions at $r = R_0$ then leads to a positive scattering length $a > R_0$ (figure 21.4b).

A concrete example is the deuteron. The reduced mass μ is equal to half the mass m of the nucleon. The matching conditions at the boundary are

$$A \sin k_i R_0 = e^{-|k|R_0} \quad \text{and} \quad A k_i \cos k_i R_0 = -|k| e^{-|k|R_0}, \quad (21.33)$$

therefore

$$\tan k_i R_0 = -\frac{k_i}{|k|} \Rightarrow \tan \sqrt{m(V_0 - B)R_0^2} = \sqrt{\frac{V_0 - B}{B}}. \quad (21.34)$$

The binding energy B of the deuteron is measured with the reaction $\gamma d \rightarrow np$ (deuteron photo-disintegration). The experiment [2] uses an x-ray source and a D_2O target. The x-rays are generated by a monoenergetic electron beam impinging on a high- Z target. The bremsstrahlung spectrum ends abruptly at the maximum x-ray energy. The deuteron binding energy is obtained by varying the electron energy and measuring the endpoint of the bremsstrahlung spectrum at which the counts in a neutron detector vanish. Neutrons are counted with a gaseous BF_3 detector, in which slow neutrons are captured with the reaction $n^{10}B \rightarrow ^7Li \alpha$. The recoiling α particle and/or the lithium ion are detected by their ionization of the gas. The result for the binding energy is $B = 2.226 \pm 0.003$ MeV [2].

One then assumes that $B \ll V_0$, which makes the right-hand side in (21.34) very large and therefore the argument of the tangent is close to $\frac{\pi}{2}$. Then in good approximation

$$\left(\frac{\pi}{2}\right)^2 = mV_0R_0^2 \Rightarrow V_0 = \frac{1}{m} \left(\frac{\pi}{2R_0}\right)^2 \simeq 50 \text{ MeV}, \quad (21.35)$$

where we have taken $R_0 = \frac{1}{m_\pi} = 1.4 \text{ fm}$ for the range of the strong interaction. The exponential decay constant

$$R = \frac{1}{\sqrt{mB}} = 4.3 \text{ fm} \quad (21.36)$$

is called the deuteron “radius”. From figure 21.4b one infers that the scattering length is equal to the sum $R + R_0$. The deuteron is a spin-1 object (3S_1 np bound state) and therefore we label the scattering length for the triplet state as $a_1 = R + R_0 = 5.7 \text{ fm}$. According to (21.29) the cross section for low energy np scattering in the triplet state should be equal to $\sigma_1 = 4\pi a_1^2 = 4.1 \text{ b}$. The latter can be measured by neutron transmission through hydrogenous liquids such as water, benzene or methanol [3], or polyethylene [4]. The np cross section is then calculated by subtracting the known contributions from carbon and oxygen. Monoenergetic neutrons can be obtained with epithermal neutrons from nuclear reactors, by exciting low energy nuclear resonances in absorbers (e.g. the 132 eV line in cobalt [4]).

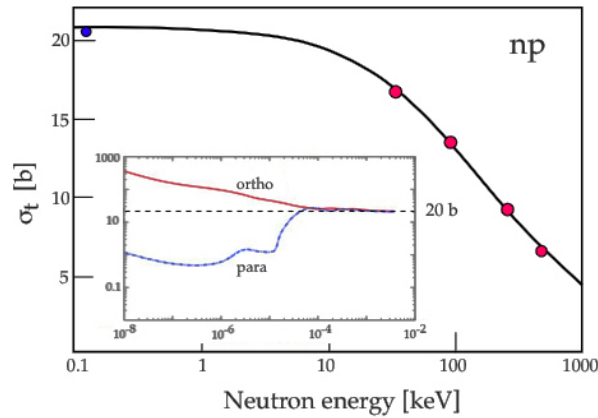


Figure 21.5: Neutron-proton total cross section as a function of neutron energy (adapted from [5]). The red dots are measurements from [3], the blue dot is from [4]. The inset shows measurements results from ortho- and para-hydrogen at 20 K (adapted from [6]).

The cross section is shown in figure 21.5. Below $\simeq 10 \text{ keV}$ the cross section reaches the constant value of 20.4 b. (Below $\simeq 1 \text{ eV}$ the cross section is influenced by chemical binding effects in the target atoms). We add the contribution σ_0 from 1S_0 scattering by averaging over the spin multiplicities, assuming unpolarized beam and target:

$$\sigma_t(np) = \frac{3}{4}\sigma_1 + \frac{1}{4}\sigma_0 = 20.4 \text{ b}, \quad (21.37)$$

hence $\sigma_0 = 69.3 \text{ b}$. The np cross section is entirely dominated by 1S_0 scattering. For the singlet scattering length one then obtains $a_0 = -23.5 \text{ fm}$ with (21.29). The negative sign

corresponds to the positive 1S_0 phase shift (see figure 21.11 below) of the attractive spin singlet potential.

The sign of a_0 can also be determined by scattering low energy neutrons from para-hydrogen molecules, in which the two proton spins are antiparallel. At very low temperatures para-hydrogen dominates over ortho-hydrogen due to its lower angular momentum ($j = 0, 2, 4, \dots$ compared to $j = 1, 3, 5, \dots$). For a sufficiently large de Broglie wavelength the contributions from the spin singlet state in para-hydrogen and from the 1S_0 np scattering amplitude interfere negatively, thus reducing the cross section substantially (inset in figure 21.5). The resulting (coherent) scattering length is equal to $\frac{3}{2}a_1 + \frac{1}{2}a_0 \simeq -3.7$ fm (for a derivation see [7]).

21.2 Resonances

We have seen in section 21.1 that for elastic scattering the internal wave function reaches its maximum amplitude at resonances, where the phase shifts passes through 90° . Let us now consider a partial amplitude $f_\ell(E)$ (equation (21.15)) with a phase increasing from $\delta_\ell = 0$ at the energy $E = 0$ (attractive potential) and passing through 90° at the energy E_0 . We follow the usual notation and express the phase shift as a function of E , the kinetic energy of the incoming particle in the center of mass system. We also assume pure elastic scattering ($\eta_\ell(E) = 1$). The **Argand diagram** (figure 21.6, left) shows how the amplitude $f_\ell(E)$ evolves in the complex plane, starting from $E = 0$.

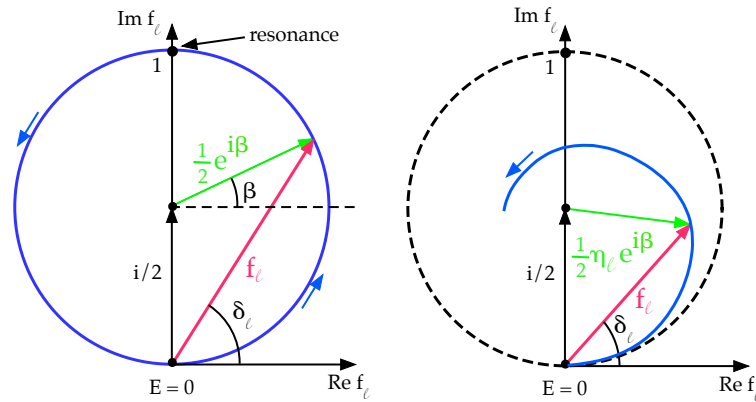


Figure 21.6: Left: Argand diagram in the complex plane for pure elastic scattering. As the energy increases from $E = 0$, the angle β increases from $-\frac{\pi}{2}$ to $\frac{3\pi}{2}$ and the angle $\delta_\ell = \frac{1}{2}(\beta + \frac{\pi}{2})$ from 0 to π . The vector $f_\ell(E)$ with modulus $|f_\ell(E)| = \sin\delta_\ell(E)$ then describes the blue circle. Right: Argand diagram in the presence of inelastic modes.

Summing the two vectors of lengths $\frac{1}{2}$ shown in the figure gives with $\beta = 2\delta_\ell - \frac{\pi}{2}$

$$\frac{i}{2} + \frac{1}{2}e^{i\beta} = \frac{i + e^{2i\delta_\ell(E)}e^{-i\frac{\pi}{2}}}{2} = \frac{e^{2i\delta_\ell(E)} - 1}{2i} = e^{i\delta_\ell(E)} \sin \delta_\ell(E) = f_\ell(E), \quad (21.38)$$

the partial amplitude (21.15). As the energy increases the vector $\frac{1}{2}e^{i\beta}$, and hence $f_\ell(E)$, describes a circle with radius $\frac{1}{2}$ (**unitarity circle**). The maximum amplitude is reached at resonance when $\delta_\ell = \frac{\pi}{2}$.

Expanding the function $\cotan \delta_\ell$ around $\delta_\ell = 90^\circ$ gives

$$\cotan \delta_\ell = 0 + \left. \frac{d \cotan \delta_\ell}{dE} \right|_{E=E_0} (E - E_0) = \frac{2}{\Gamma} (E_0 - E), \quad (21.39)$$

where we have defined the width Γ of the resonance as

$$\Gamma \equiv - \frac{2}{\left. \frac{d \cotan \delta_\ell}{dE} \right|_{E=E_0}} > 0. \quad (21.40)$$

Let us rewrite the partial wave amplitude (21.15) as

$$\begin{aligned} f_\ell(E) &= e^{i\delta_\ell} \sin \delta_\ell = \cotan \delta_\ell \sin^2 \delta_\ell + i \sin^2 \delta_\ell \\ &= (\cotan \delta_\ell + i) \times \underbrace{\sin^2 \delta_\ell}_{= \frac{1}{1 + \cotan^2 \delta_\ell} = \frac{1}{(\cotan \delta_\ell + i)(\cotan \delta_\ell - i)}} \\ &= \frac{1}{\cotan \delta_\ell - i}, \end{aligned} \quad (21.41)$$

which leads with (21.39) to

$$f_\ell(E) = \frac{1}{\frac{2}{\Gamma}(E_0 - E) - i}. \quad (21.42)$$

If the resonance is produced in the partial wave ℓ and is strong enough to fully dominate the cross section, the elastic cross section (21.14) becomes

$$\sigma_e = \frac{4\pi}{k^2} (2\ell + 1) \left| \frac{1}{\frac{2}{\Gamma}(E_0 - E) - i} \right|^2 = \frac{\pi K}{k^2} \left[\frac{\Gamma^2}{(E - E_0)^2 + \frac{\Gamma^2}{4}} \right], \quad (21.43)$$

with $K \equiv 2\ell + 1$. We have recovered the Breit-Wigner distribution (4.28). However, our derivation made no assumption about spins. Comparing with (12.90) we have to replace $2\ell + 1$ in (21.43) by $2j + 1$ to take into account the spin j of the resonance, and also average over the projectile and target spins, assuming that they are unpolarized. Therefore

$$K = \frac{2j + 1}{(2s_1 + 1)(2s_2 + 1)}. \quad (21.44)$$

The resonance energy E_0 is the point at which the phase δ_ℓ varies most rapidly (figure 21.7).

The situation is more complicated in the presence of inelastic modes and when $\eta_\ell(E)$ is also a function of the energy. In this case the path described by the amplitude $f_\ell(E)$ is entirely contained within the unitarity circle (figure 21.6, right). Resonances also occur at energies when the phase δ_ℓ moves most rapidly with energy. However, a resonance does not necessarily lead to a maximum $|f_\ell(E_0)|$ (an example will be shown below in figure 21.9 below).

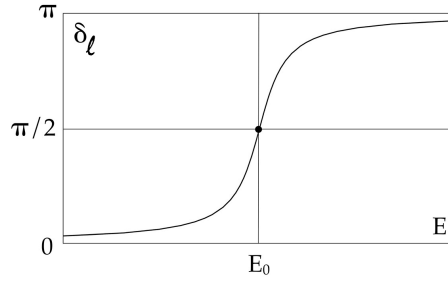


Figure 21.7: The phase shift δ_ℓ (calculated with (21.39)) varies most rapidly at the resonance energy E_0 .

Let us now assume a resonance occurring at $\delta_\ell = \frac{\pi}{2}$ with inelasticity $\eta_\ell < 1$ that does not vary noticeably over the resonance range. Produced in the partial wave ℓ , the resonance decays elastically with partial width Γ_e , but also into further channels with partial width Γ_r , hence $\Gamma = \Gamma_e + \Gamma_r$. One finds the elastic resonance cross section by multiplying $f_\ell(E)$ in (21.42) with the branching ratios $x \equiv \frac{\Gamma_e}{\Gamma}$:

$$\sigma_e = \frac{\pi K}{k^2} \left[\frac{x^2 \Gamma^2}{(E - E_0)^2 + \frac{\Gamma^2}{4}} \right] = \frac{\pi K}{k^2} \left[\frac{\Gamma_e^2}{(E - E_0)^2 + \frac{\Gamma^2}{4}} \right]. \quad (21.45)$$

The cross section for resonance excitation by particles 1 + 2 **and** for subsequent decay into 1 + 2 is proportional to Γ_e^2 (that is proportional to the square of the branching ratio $\frac{\Gamma_e}{\Gamma}$ for decay into 1 + 2). On the other hand, the total cross section for resonance excitation is obtained from the optical theorem (21.19):

$$\sigma_t = \frac{4\pi}{k^2} K x \text{Im} f_\ell(E) = \frac{\pi K}{k^2} \left[\frac{x \Gamma^2}{(E - E_0)^2 + \frac{\Gamma^2}{4}} \right] = \frac{\pi K}{k^2} \left[\frac{\Gamma_e \Gamma}{(E - E_0)^2 + \frac{\Gamma^2}{4}} \right]. \quad (21.46)$$

The difference $\sigma_t - \sigma_e$ is equal to the the reaction cross section

$$\sigma_r = \frac{\pi K}{k^2} \left[\frac{\Gamma_e \overbrace{(\Gamma - \Gamma_e)}^{\equiv \Gamma_r}}{(E - E_0)^2 + \frac{\Gamma^2}{4}} \right] = \frac{\pi K}{k^2} \left[\frac{\Gamma_e \Gamma_r}{(E - E_0)^2 + \frac{\Gamma^2}{4}} \right], \quad (21.47)$$

as advertised in (10.55). The cross section σ_t for resonance excitation by particles 1 + 2 and decay into **all** allowed channels is proportional to $\Gamma_e \Gamma$. The cross section σ_r for resonance excitation and decay into all channels, but 1 + 2, is proportional to $\Gamma_e \Gamma_r$.

21.3 Some examples of partial wave analyses

Partial wave expansions are useful to parametrize the interaction, but also to uncover new resonances and to measure their quantum numbers, as the following examples illustrate. Let us first examine the scattering of α particles off ^4He nuclei. The symmetry of the wave function for a pair of spin-0 particles restricts the relative angular momentum ℓ to be even. Figure 21.8 (left) shows examples of the differential cross section measured at

various laboratory kinetic energies below 120 MeV. The process is inelastic due to nuclear reactions such as $\alpha\alpha \rightarrow {}^7\text{Li}p$ or $\alpha\alpha \rightarrow {}^7\text{Be}n$. Fitting the scattering amplitude (21.12) to the differential cross section leads to the phase shifts shown in figure 21.8 (right). (The well known phase shifts due to the Coulomb potential have to be taken into account.) Starting from 180° the δ_0 phase decreases with energy due to the ${}^8\text{Be}$ bound state, akin to the behaviour of the 3S_1 phase in np scattering which is due to the deuteron bound state. At low energies (hence large distances) the phases are positive and thus correspond to an attractive potential. At higher energies the low angular momentum phases δ_0 and δ_2 change sign, thus the potential becomes repulsive at short distance. Some of the phases are resonant, in particular δ_2 and δ_4 due to the 2.9 MeV 2^+ and 11.7 MeV 4^+ excited states of ${}^8\text{Be}$, respectively.

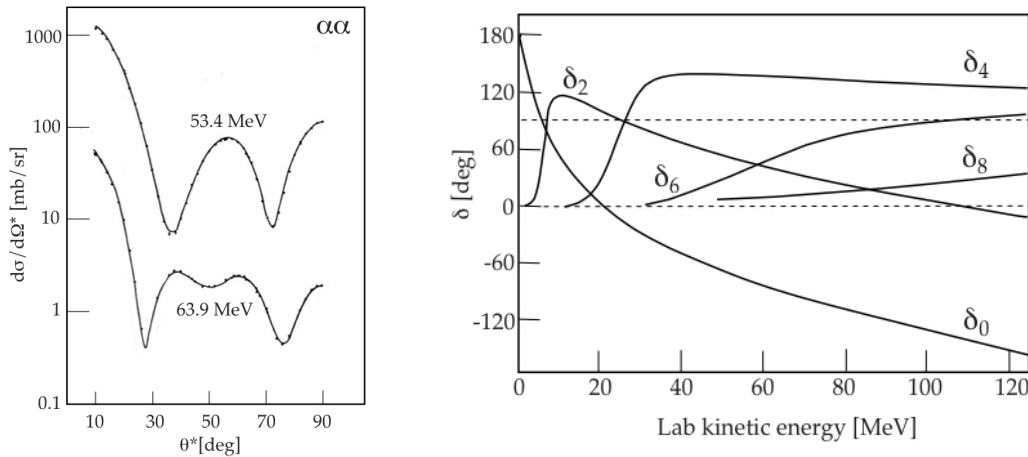


Figure 21.8: Left: Differential cross section for $\alpha\alpha$ scattering in the center-of-mass system for two α energies in the laboratory. Right: phase shifts as a function of laboratory kinetic energy (twice the center-of-mass energy) (adapted from [8]).

The $\pi\pi \rightarrow \pi\pi$ scattering is another example involving two spin-0 particles scattering and also inelastic channels. This process can be analyzed by using πp scattering in which the exchange pion acts as target particle and a pion pair (see figure 12.17) or a $K\bar{K}$ pair is produced. Figure 21.9 shows the Argand diagram of the $\pi\pi$ S -wave (see also [9]). The modulus of the amplitude f_0 reaches its maximum value around 850 MeV, loops back and passes rapidly through the $f_0(980)$ meson resonance near the $\pi\pi \rightarrow K\bar{K}$ threshold (990 MeV) where it reaches its **minimum** value, before starting a new inelastic loop. The $f_0(980)$ scalar ($J^{PC} = 0^{++}$) meson then does not appear as a Breit-Wigner peak but as a hole in the $\pi\pi$ invariant mass distribution of $\bar{p}p \rightarrow 3\pi^0$ [10].

Our next example is pion-nucleon scattering that was already dealt with in section 12.4.2. Here the formalism is slightly more complicated due to the two isospins, $\frac{1}{2}$ and $\frac{3}{2}$, and the nucleon spin. The πN phase shifts are obtained from measurements of the total and differential cross sections, complemented by data on the analysing power (see figure 11.4 and equation (11.31)). A detailed derivation of the formalism can be found in

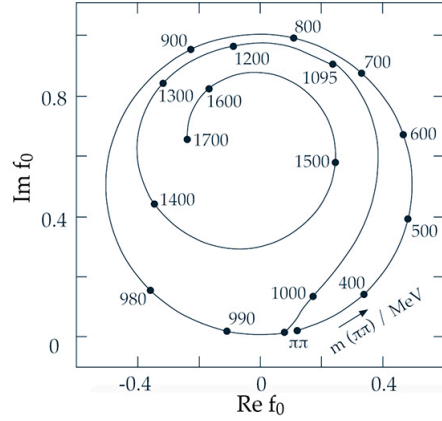


Figure 21.9: Argand diagram of the $\ell = 0$ $\pi\pi$ scattering amplitude from a common fit to scattering data and production in $\bar{p}p$ annihilation into $3\pi^0$ (from [12]).

[13]. The total cross section is given by

$$\sigma_t = \frac{4\pi}{k^2} \sum_{j=\frac{1}{2}}^{\infty} \left[\sum_{\ell=j-1}^{\ell=j+1} \left(j + \frac{1}{2} \right) |f_{\ell j}(k)|^2 \right], \quad (21.48)$$

where $f_{\ell j}(k)$ is given by (21.15) with the phase shift now depending also on $j = \ell \pm 1$. The process is described by $f(\theta)$ and by the spin-flip amplitude $g(\theta)$:

$$\begin{aligned} f(\theta) &= \frac{1}{k} \sum_{\ell=0}^{\infty} [(\ell+1)f_{\ell j+\frac{1}{2}} + \ell f_{\ell j-\frac{1}{2}}] P_{\ell}(\cos(\theta)), \\ g(\theta) &= -\frac{1}{k} \sum_{\ell=1}^{\infty} [f_{\ell j+\frac{1}{2}} - f_{\ell j-\frac{1}{2}}] \frac{dP_{\ell}(\cos(\theta))}{d\cos\theta} \sin\theta, \end{aligned} \quad (21.49)$$

where $P_{\ell}(\cos\theta)$ are Legendre polynomials. The differential cross section is given by

$$\frac{d\sigma}{d\Omega} = |f(\theta)|^2 + |g(\theta)|^2. \quad (21.50)$$

The analyzing power (11.31) is usually denoted as $P(\theta)$ and is given by

$$P(\theta) \equiv a(\theta) = \frac{2 \operatorname{Im} f^* g}{|f|^2 + |g|^2}. \quad (21.51)$$

For π^+p scattering the isospin is $i = \frac{3}{2}$, while for π^-p both $\frac{1}{2}$ and $\frac{3}{2}$ contribute. Hence $f(\theta)$ and $g(\theta)$ have to be calculated separately for $\frac{1}{2}$ and $\frac{3}{2}$, then added coherently following (12.88). For example, for $\pi^-p \rightarrow \pi^0 n$ the amplitude $f(\theta)$ would read

$$f(\theta) = \frac{\sqrt{2}}{3} f_{\frac{3}{2}}(\theta) - \frac{\sqrt{2}}{3} f_{\frac{1}{2}}(\theta), \quad (21.52)$$

and likewise for $g(\theta)$. The amplitudes also need to be corrected for the Coulomb interaction [14].

The total cross sections are shown in figure 12.15 for π^+p and π^-p scattering. Figure 21.10 illustrates the energy dependence of the phase shifts in the lowest partial waves. They depend on ℓ , i and j and are usually labelled $\ell_{2i+1} 2j+1$. The low energy region is dominated by the $J^P = \frac{3}{2}^+ \Delta(1232)$ baryon, as can be seen from the resonating $I(J^P) = \frac{3}{2}(\frac{3}{2}^+) P_{33}$ wave. The P_{11} and D_{13} amplitudes also resonate at the masses of the $I(J^P) = \frac{1}{2}(\frac{1}{2}^+)$ and $I(J^P) = \frac{1}{2}(\frac{3}{2}^-)$ baryons.

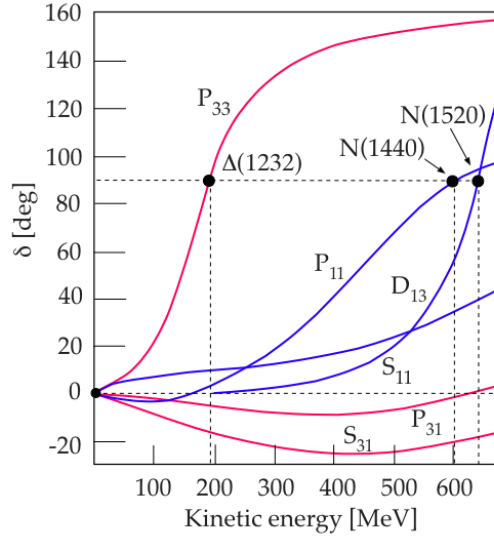


Figure 21.10: The lowest pion-nucleon phase shifts as a function of laboratory kinetic energy. The red curves correspond to $i = \frac{3}{2}$, the blue ones to $i = \frac{1}{2}$ (adapted from [15], where phase shifts for higher partial waves can be found).

Finally, let us deal with nucleon-nucleon scattering. Owing to the spins and isospins of the proton and neutron the expansion in terms of partial waves is even more complicated. The isospin $i=1$ contributes to pp , np and nn scattering, while $i = 0$ contributes only to np . According to the selection rule (12.76), for ℓ even the spin singlet (triplet) amplitude occurs in the isospin triplet (singlet) states, while for ℓ odd the spin singlet (triplet) contributes to the isospin singlet (triplet) states. This leads to the following energy dependent phase shifts, using the notation $^{2s+1}\ell_j$:

$$\begin{aligned}
 pp, nn & : \ ^1S_0, \ ^3P_0, \ ^3P_1, \ ^3P_2, \ ^1D_2 \dots \\
 np & : \ ^1S_0, \ ^3P_0, \ ^3P_1, \ ^3P_2, \ ^1D_2 \text{ and } \ ^3S_1, \ ^1P_1, \ ^3D_1, \ ^3D_2, \ ^3D_3 \dots
 \end{aligned} \quad (21.53)$$

There are additional parameters describing the mixing of partial amplitudes with the same parity and the same total angular momentum j , such as 3S_1 and 3D_1 . Figure 21.11 shows the energy dependence of the 1S_0 and 3S_1 phases. At low energies (hence large distances) the 1S_0 phase is positive and remains smaller than 90° . The attractive force is not quite sufficient to bind the two nucleons in the isotriplet state, in contrast to the 3S_1 isosinglet state. There is no pp sibling of the deuteron and also no low energy nucleon-nucleon resonance.

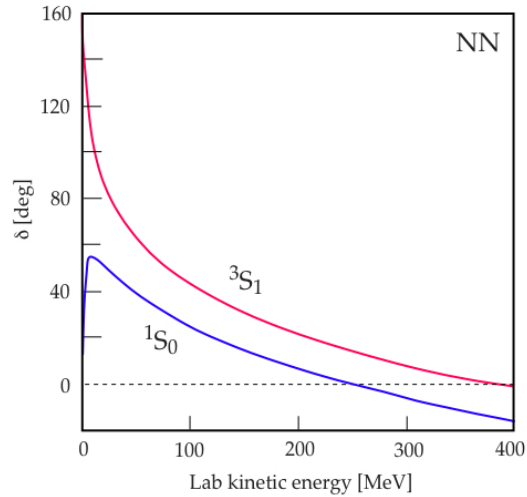


Figure 21.11: Isotriplet 1S_0 and isosinglet 3S_1 nucleon-nucleon phase shifts as a function of laboratory energy.

The numerous higher partial waves cannot be determined unambiguously from differential cross section measurements only. Additional information is obtained from spin observables. One measures left-right asymmetries with a polarized beam or a polarized target and determines the polarizations of the outgoing nucleons.

Figure 21.12 shows as an example one of the neutron-proton scattering experiments performed at the TRIUMF isochronous cyclotron with neutrons between 200 and 500 MeV [16]. The polarized proton beam with an energy between 183 and 520 MeV impinges on a liquid deuterium target (LD_2) to produce neutrons. The proton beam is then directed towards the beam dump by a bending magnet. A polyethylene target is inserted into the proton beam to monitor its polarization from the known analysing power in pp scattering. The typical proton polarization is 78%. The emerging neutron beam is fairly monoenergetic (~ 10 MeV wide) due to the final state interaction between the two protons recoiling slowly in the laboratory [11]. Furthermore, a high transfer of proton to neutron polarization ($\simeq 81\%$ for a scattering angle of 9° at 237 MeV) is obtained with transversely polarized protons. The direction of the proton polarization is therefore rotated into the horizontal plane by a superconducting solenoid.

The horizontally polarized neutron beam is collimated before passing through a dipole magnet with vertical field to rotate the neutron spin in the horizontal plane. The neutrons then fly through a further dipole magnet with horizontal field to obtain a vertical component of the neutron polarization. The scattered neutrons in the liquid hydrogen target (LH_2) are detected by an array of thick scintillation counters. The recoil protons are detected in coincidence by the proton polarimeter, made of scintillation counters and multiwire proportional chambers. A graphite target is inserted to measure the proton polarization from the scattering asymmetry in carbon, using the known pC analysing power.

The setup allows neutrons to be polarized in any direction before striking the liquid hydrogen target. Figure 21.12 shows the measurement of D_t , one of the **triple scattering**

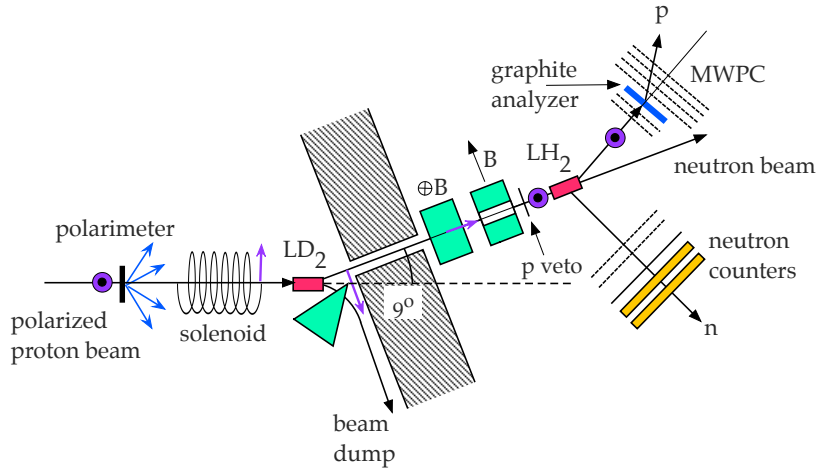


Figure 21.12: Setup to measure spin observables in np scattering (see the text) [16]. For the measurement of the parameters P and D_t the magnetic fields of the dipole magnets are tuned to orient the neutron polarization into the vertical direction.

(or Wolfenstein) spin parameters, which enters the polarization transfer to the proton when the neutron spin is perpendicular to the scattering plane. The polarization of the recoil proton is given by [16]

$$\langle \sigma_p \rangle = \frac{-P(\theta) \pm D_t(\theta) \langle \sigma_n \rangle}{1 \mp P(\theta) \langle \sigma_n \rangle}, \quad (21.54)$$

where θ refers to the center-of-mass frame and $\langle \sigma_n \rangle$ is the vertical polarization of the incident neutron. The parameter $P(\theta)$ is the analysing power in np scattering which can be obtained by measuring the left-right scattering asymmetry at the hydrogen target. Figure 21.13 shows the angular distribution of the parameters $P(\theta)$ and $D_t(\theta)$ for 425 MeV neutrons.

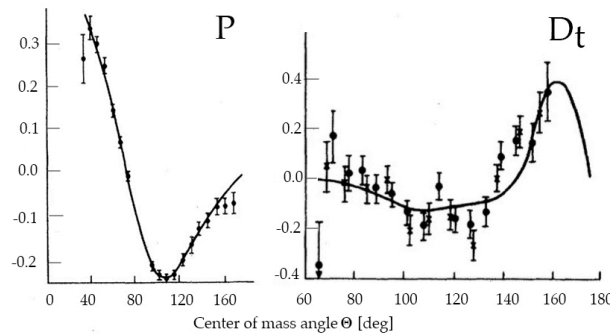


Figure 21.13: The Wolfenstein parameters $P(\theta)$ and $D_t(\theta)$ measured in np scattering at 425 MeV (adapted from [16]).

The formalism which relates the analysing power and spin observables to the nucleon-nucleon phase shifts can be found in [17]. The phase shifts have been determined between 200 and 500 MeV up to the $\ell = 5$ (H) waves [18]. There is no indication for nucleon-

nucleon (**dibaryon**) resonances below 500 MeV. Evidences for dibaryons at higher energies have been reported, in particular for an isospin singlet $J^P = 3^+$ state $d^*(2380)$, produced with polarized neutrons around 1140 MeV, and decaying into $d\pi^+\pi^-$ and $d\pi^0\pi^0$ [19].

21.4 Scattering of ultracold neutrons

Figure 21.3 above shows that most nuclei are repulsive for very low energy neutrons. This was first noticed by Fermi [20] and demonstrated experimentally in 1947 (figure 21.14). Monoenergetic neutrons are obtained by Bragg-scattering of thermal neutrons (average energy of 26 meV) from the Argonne nuclear reactor. The neutrons are collimated towards a beryllium mirror, the surface of which is inclined by the glancing angle θ (figure 21.14 left). The intensity of the reflected beam under the angle θ (specular reflection) is then recorded by a BF_3 counter located at the angle θ .

Figure 21.14 (right) shows the measured intensities as a function of detector position for various glancing angles θ . One observes a rapid drop of the reflected intensity around $\theta_c \sim 12'$ (arcminutes), the critical angle at which total reflection occurs. We will show below that total reflection occurs for $\sin \theta_c \leq \sqrt{V/T}$, where V is a repulsive potential and T the kinetic energy of the neutron. For beryllium $V = 252$ neV, while for thermal neutrons $T \simeq 26$ meV, hence the glancing angle is very small, $\theta_c \sim 11'$, as observed. Thus, with slower neutrons one expects θ_c to increase.

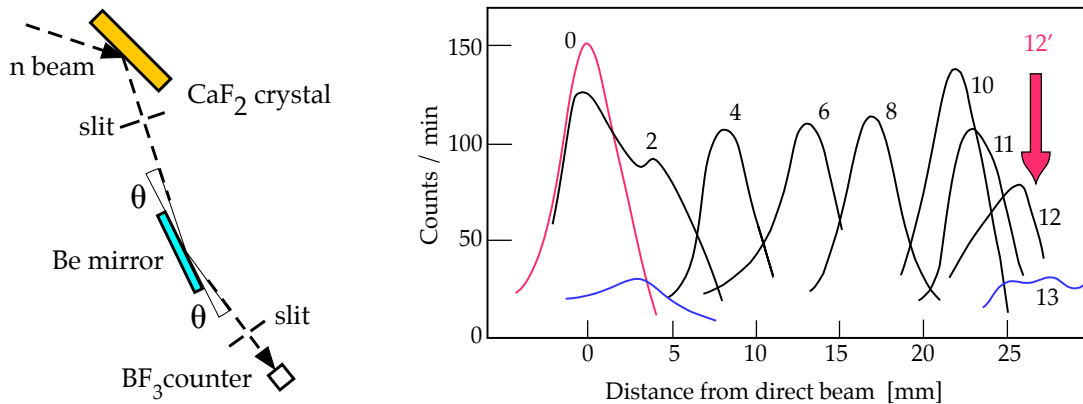


Figure 21.14: Left: setup to demonstrate the total reflection of thermal neutrons by a beryllium mirror. Right: neutron intensity as a function of detector distance from the direct beam, for various glancing angles in arcminutes. The red distribution corresponds to the direct beam, while the blue curves show background measurements (adapted from [20]).

Total reflection occurs at any incident angle ($\theta_c = 90^\circ$) when $T < V$. **Ultracold** neutrons (UCN) have energies below 300 neV. These neutrons can therefore be transported in evacuated tubes and stored in vacuum vessels coated with suitable materials, with minimal losses. They are of great interest to study properties of the neutron, such as its β -decay, its lifetime (section 13.1.1) and electric dipole moment (section 11.8). Table 21.1 compares typical values for slow neutrons in the three main energy regimes. We have replaced the

reduced mass μ by the mass m of the neutron since the neutron scatters off bound nuclei at the surface of the material. To fix ideas, a 100 neV neutron launched vertically at the surface of the Earth will reach the altitude $h = 100 \text{ neV/mg} \simeq 1 \text{ m}$. For details on UCN physics see [21, 22]).

Table 21.1: Typical values for the velocity, energy and de Broglie wavelength of slow neutrons ($m = 939.6 \text{ MeV}$, $1 \text{ fm}^{-1} = 197.3 \text{ MeV}$). The kinetic energy of thermal neutrons corresponds to $k_{\text{Boltzmann}} \times 300 \text{ K} = 26 \text{ meV}$.

	Velocity [m/s] $v = \beta c$	Energy [meV] $T = \frac{1}{2}m\beta^2$	Wavelength [nm] $\lambda = \frac{2\pi}{m\beta}$
Thermal	2232	26	0.18
Cold	438	1	0.89
Ultracold	4.4	100 neV	89

To calculate the critical angle as a function of neutron energy we need an ansatz for the repulsive potential which leads to a scattering amplitude satisfying (21.31) for very low energy neutrons. The relation between potential and scattering amplitude is given in first order perturbation by the Born approximation, valid only for weak forces. This cannot be applied to our strong square-well potential. (e.g. because of multiple scattering). Nonetheless, let us sketch a derivation of the Born approximation starting from the golden rule (13.25), which states that the transition rate (scattering rate) is given by

$$\frac{d\Gamma}{dT} = 2\pi|\mathcal{M}|^2 \frac{dn}{dT} = 2\pi|\mathcal{M}|^2 \frac{k^2}{2\pi^2} \frac{dk}{dT} = |\mathcal{M}|^2 \frac{mk}{\pi}, \quad (21.55)$$

where we have used (13.26) for dn and the relation $T = k^2/2m$, hence $dk = m dT/k$. The (isotropic) differential cross section is obtained by dividing by the flux per unit solid angle ($4\pi v$):

$$\frac{d\sigma}{d\Omega} = \frac{d\Gamma}{dT} \frac{1}{4\pi v} = \frac{m^2}{4\pi^2} |\mathcal{M}|^2 = |f(\theta)|^2. \quad (21.56)$$

In first order perturbation theory the transition amplitude would be given by

$$\mathcal{M} = \int (e^{i\vec{k}'\vec{r}})^* V(r) e^{i\vec{k}\vec{r}} d^3\vec{r} = \int V(r) e^{i\vec{q}\vec{r}} d^3\vec{r}, \quad (21.57)$$

where we have written the incident and outgoing wave functions as plane waves and $\vec{q} = \vec{k} - \vec{k}'$. Therefore the scattering amplitude would read with (21.56)

$$f(\theta) = -\frac{m}{2\pi} \int V(r) e^{i\vec{q}\vec{r}} d^3\vec{r}, \quad (21.58)$$

in Born approximation. (We have chosen the minus sign since for a weak repulsive potential $V(r) = V_0 > 0$ (hence $a > 0$) the scattering amplitude is negative for $q \rightarrow 0$, in

accord with $f = -a$ (21.31).) However, this cannot be applied to strong interactions. The ansatz for a potential that would lead to (21.31) and (21.32) is

$$V(\vec{r}) = \frac{2\pi}{m} a \delta(\vec{r}), \quad (21.59)$$

as can easily be verified by inserting into (21.58). This is the Fermi **pseudo-potential**, a mathematical construct to be used only with the Born approximation.

Now, in our derivation we have considered scattering off a single atom located at $\vec{r} = 0$, while table 21.1 shows that for UCN the de Broglie wavelength is much larger than the size of the atom and even larger than the typical lattice constant in a solid material. We therefore have to rewrite (21.2) by summing coherently over all neighbouring atoms located at positions \vec{r}_i , assuming that the material is homogeneous. The derivation, see [21] p17, gives

$$V(\vec{r}) = \frac{2\pi}{m} a \sum_i \delta(\vec{r} - \vec{r}_i) = \frac{2\pi}{m} a N(\vec{r}), \quad (21.60)$$

where $N(\vec{r})$ is the atomic density and a the **coherent** bound atom scattering length.

Let us now consider slow neutrons (kinetic energy T) incident on a smooth surface (figure 21.15, left). Total (specular) reflection occurs when the energy orthogonal to the surface is equal to

$$T_{\perp} \equiv \frac{1}{2} m (v \sin \theta)^2 \leq V = \frac{2\pi}{m} a N \quad (21.61)$$

that is for glancing angles θ smaller the angle θ_c given by

$$\sin \theta_c \equiv \lambda \sqrt{\frac{aN}{\pi}} = \sqrt{\frac{V}{T}}. \quad (21.62)$$

For example, for the experiment with thermal neutrons shown in figure 21.14, one obtains from a measurement of the limiting glancing angle the potential $V \simeq 250$ neV and the scattering length $a = 8.9$ fm for the scattering of neutrons off beryllium [20].

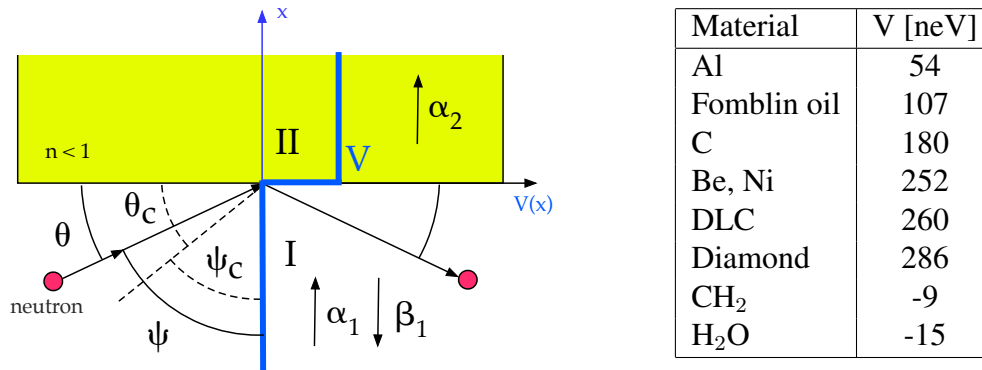


Figure 21.15: Left: Total reflection of ultra-cold neutrons with glancing angle θ below θ_c . Right: Fermi pseudo-potential for various materials. DLC (diamond-like carbon) is an amorphous carbon material which has properties such as slickness and hardness similar to diamond.

Recall that total internal reflection with light occurs at the interface between a transparent medium and vacuum, when the incident angle ψ is larger or equal to ψ_c (figure 21.15, left), where $\sin \psi_c = \frac{1}{n}$ and n is the refractive index of the medium (Snell's law). In contrast, the neutron propagates in vacuum towards a reflecting surface with "refractive index" n for neutrons. The condition for total reflection now reads $\psi \geq \psi_c$ where $\sin \psi = n$ which means that the refractive index must be **smaller** than one. For the glancing angle θ_c one gets

$$\sin \theta_c = \cos \psi_c = \sqrt{1 - \sin^2 \psi_c} = \sqrt{1 - n^2} \Rightarrow n = \sqrt{1 - \frac{V}{T}} \leq 1 \quad (21.63)$$

and hence

- For $T > V$ there is a limiting glancing angle given by (21.62). The refractive index is $0 < n < 1$.
- For $T = V$ total reflection occurs at all angles and $n = 0$.
- For $T < V$, that is for velocities lower than the critical velocity

$$v_c \equiv \frac{1}{m} \sqrt{4\pi a N}, \quad (21.64)$$

the neutrons are reflected at **any** angle and n becomes imaginary.

The table in figure 21.15 lists values of the Fermi pseudo-potential. Note the negative values for hydrogenous materials which are due to the attractive np potential discussed at the end of section 21.1.1.

In the presence of an external magnetic field the neutron energy is modified by the interaction with the neutron magnetic dipole moment

$$V_m = \pm \mu_n B = \pm \frac{g_n}{2} \mu_N B \Rightarrow \boxed{V_m [\text{neV}] = \pm 60 B [\text{T}]}, \quad (21.65)$$

where μ_N is the nuclear magneton, see (2.45). This term is added to the Fermi potential V , e.g. in (21.61), and leads to two different limiting glancing angles, depending on the sign of the magnetic field. With a proper choice of the reflection angle one can then separate neutrons with opposite spin orientations and produce polarized neutron beams.

We now calculate the reflection probability for ultracold neutrons with energies $T < V$. Losses can be due to surface roughness which leads to non-specular reflection, or to nuclear excitation. Neutrons may also receive enough energy from vibrating atoms to overcome the Fermi potential barrier. Therefore the mirror needs to be operated at temperatures as low as a few kelvins to reduce this thermal "up-scattering" effect. To begin with, let us ignore losses and calculate the reflectivity from the step potential shown in figure 21.15 (left). The component of the kinetic energy perpendicular to the reflecting surface is $T_\perp = \frac{1}{2} m v_\perp^2 = T \sin^2 \theta$. The solutions of the one-dimensional Schrödinger equation (see equation (5.19)) read for $T_\perp < V$

$$\psi_I(x) = \alpha_1 e^{ik_1 x} + \beta_1 e^{-ik_1 x} \quad \text{and} \quad \psi_{II}(x) = \alpha_2 e^{-k_2 x} \quad (21.66)$$

in the regions I and II. The incident wave has amplitude α_1 , the reflected one amplitude β_1 . The (real) wave numbers are

$$k_1 = \sqrt{2mT_\perp} \quad \text{and} \quad k_2 = \sqrt{2m(V - T_\perp)}, \quad (21.67)$$

respectively. Continuity at the surface requires that

$$\alpha_2 = \alpha_1 + \beta_1 \quad \text{and} \quad \alpha_1 i k_1 - \beta_1 i k_1 = -k_2 \alpha_2. \quad (21.68)$$

Eliminating α_2 gives the ratio of amplitudes

$$R \equiv \frac{\beta_1}{\alpha_1} = \frac{k_1 - i k_2}{k_1 + i k_2} \quad (21.69)$$

and hence the reflectivity

$$|R|^2 = \left| \frac{\beta_1}{\alpha_1} \right|^2 = \left| \frac{k_1 - i k_2}{k_1 + i k_2} \right|^2 = 1, \quad (21.70)$$

as expected for an infinitely broad potential barrier. Let us now include small reflectivity losses by adding to the potential a small imaginary part, and write $V \equiv U - iW$ where $W \ll U$. The imaginary part then leads to a plane wave contribution to ψ_{II} in (21.66). The reflectivity becomes with $k_2 = \sqrt{2m\sqrt{U - T_\perp - iW}}$ and $\Delta \equiv U - T_\perp$

$$\begin{aligned} R &= \frac{\sqrt{T_\perp} - i\sqrt{\Delta - iW}}{\sqrt{T_\perp} + i\sqrt{\Delta - iW}} = \frac{\sqrt{T_\perp} - i\sqrt{(1 - \frac{iW}{\Delta})\Delta}}{\sqrt{T_\perp} + i\sqrt{(1 - \frac{iW}{\Delta})\Delta}} \\ &\simeq \frac{\sqrt{T_\perp} - i\sqrt{\Delta}(1 - \frac{iW}{2\Delta})}{\sqrt{T_\perp} + i\sqrt{\Delta}(1 - \frac{iW}{2\Delta})} = \frac{\sqrt{T_\perp} - \frac{W}{2\sqrt{\Delta}} - i\sqrt{\Delta}}{\sqrt{T_\perp} + \frac{W}{2\sqrt{\Delta}} + i\sqrt{\Delta}} \end{aligned} \quad (21.71)$$

for $W \ll \Delta$. The modulus gives, when ignoring terms quadratic in W ,

$$\begin{aligned} |R|^2 &= \frac{T_\perp - \sqrt{\frac{T_\perp}{\Delta}}W + \Delta}{T_\perp + \sqrt{\frac{T_\perp}{\Delta}}W + \Delta} = \frac{U - \sqrt{\frac{T_\perp}{\Delta}}W}{U + \sqrt{\frac{T_\perp}{\Delta}}W} = \frac{1 - \sqrt{\frac{T_\perp}{\Delta}}\frac{W}{U}}{1 + \sqrt{\frac{T_\perp}{\Delta}}\frac{W}{U}} \\ &\simeq \left(1 - \sqrt{\frac{T_\perp}{\Delta}}\eta\right)^2 \simeq 1 - 2\eta\sqrt{\frac{T_\perp}{U - T_\perp}}, \end{aligned} \quad (21.72)$$

with $\eta \equiv \frac{W}{U}$. The reflection probability **per bounce** for UCN with $T_\perp < U$ is then given by

$$\boxed{|R|^2 = 1 - 2\eta\sqrt{\frac{T \sin^2 \theta}{U - T \sin^2 \theta}}}. \quad (21.73)$$

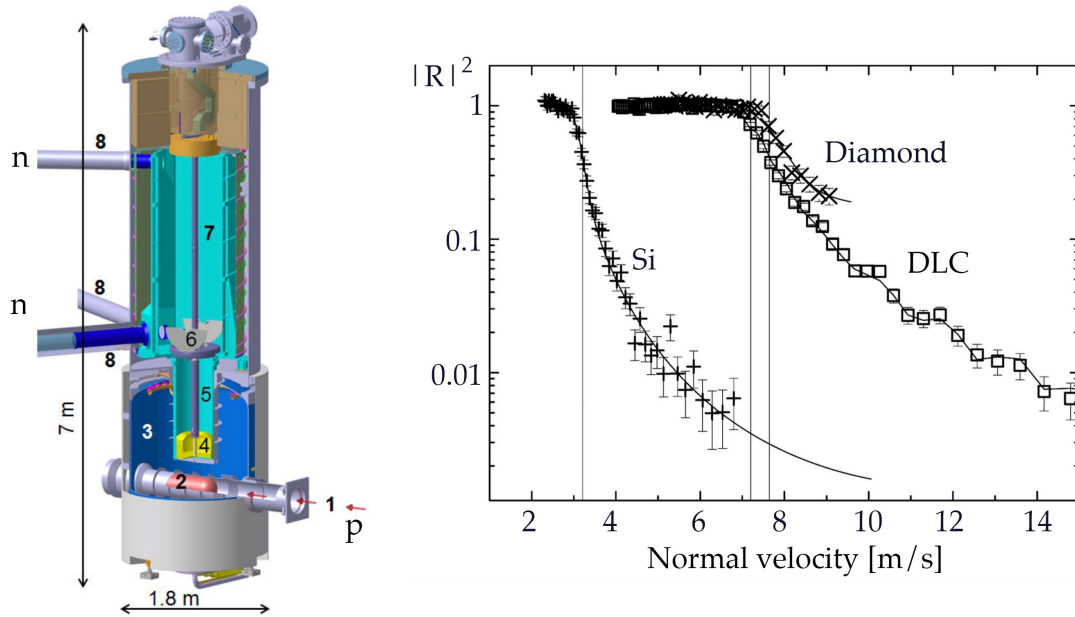


Figure 21.16: Left: sketch of the UCN source at PSI; 1-proton beam, 2-spallation target, 3-D₂O moderator, 4-solid D₂ moderator, 5-vertical UCN guide, 6-shutter, 7-UCN storage vessel, 8-neutron guides to the experiments (from [23]). Right: neutron reflectivity of silicon (+), DLC coating (open squares) and diamond (x). The lines are fits (the oscillating curve for DLC is due to interferences with the substrate). The vertical lines give the expected values for the critical velocities (after [24]).

The material parameter η can be obtained from the neutron storage time in a bottle with inner walls coated with the corresponding material. The losses $1 - |R|^2$ lie typically in the range $2\eta = 10^{-4} - 10^{-3}$, increasing slightly towards large glancing angles.

Figure 21.16 (left) shows the high intensity UCN source at the spallation source of the Paul-Scherrer Institute in Switzerland. Neutrons are produced by the high intensity 590 MeV proton beam impinging on a lead target. Short beam pulses of 4 s hit the target every 400 s, during which time the neutrons can be moderated and stored. About 8 neutrons are produced by each incident proton and the neutron intensity is 10^{17} s^{-1} . The neutrons are thermalized with heavy water and further cooled by a solid 30 dm³ D₂ moderator operated at a temperature of 5 K. The neutrons are then trapped in the vertical container by closing the bottom shutter.

Figure 21.16 (right) shows the reflectivity measured at the PSI spallation source for Si, DLC and diamond, as a function of velocity perpendicular to the surface. DLC with $V \simeq 260 \text{ neV}$ performs only slightly worse than diamond and has been chosen as coating material for the storage vessel, which is kept at a temperature below 100 K. The neutron density is around 1000 UCN/cm³.

References

- [1] Mayer-Kuckuk T 1984 *Kernphysik* (Stuttgart:Teubner)
- [2] Mobley R C and Laubenstein R A. *Phys. Rev.* **80** (1950) 309

- [3] Frisch D H *Phys. Rev.* **70** (1946) 589
- [4] Dilg W *Phys. Rev.* **C 11** (1975) 103
- [5] Bohm D and Richman C *Phys. Rev.* **71** (1947) 567
- [6] Grammer K B *et al.* *Phys. Rev.* **B 91** (2015) 180301(R)
- [7] Blatt M and Weisskopf V F 1979 *Theoretical Nuclear Physics* (New York:Dover)
- [8] Darriulat P *et al.* *Phys. Rev.* **137** (1965) B 315
- [9] Au K L, Morgan D, Pennington M R *Phys. Rev.* **D 35** (1987) 1633
- [10] Amsler C *et al.* *Phys. Lett.* **B 342** (1995) 433
- [11] Amsler C *et al.* *Nucl. Instrum. Methods* **157** (1978) 203
- [12] Spanier S 1994 *PhD Thesis* (Universität Mainz)
- [13] Williams W S C 1971 *An Introduction to Elementary Particles* (New York:Academic)
- [14] Mott N F and Massey H S W 1965 *The theory of Atomic Collisions* (Oxford: Oxford University Press)
- [15] Roper LD, Wright R M and Feld B T *Phys. Rev.* **138** (1965) B 190
- [16] Clough A S *et al.* *Phys. Rev.* **C 21** (1980) 988
- [17] Hoshizaki N *Suppl. Prog. Theor. Phys.* **42** (1968) 107
- [18] Bugg D V *et al.* *Phys. Rev.* **C 21** (1980) 1004
- [19] Adlarson P *et al.* *Phys. Rev. Lett.* **112** (2014) 202301
- [20] Fermi E and Marshall L *Phys. Rev.* **71** (1947) 666
- [21] Golub R, Richardson D J, Lamoreaux S K 1991 *Ultra-Cold Neutrons* (Bristol: Hilger)
- [22] Golub R and Pendlebury J M *Rep. Prog. Phys.* **42** (1979) 439
- [23] Becker H *et al.* *Nucl. Instrum. Methods Phys. Res. A* **777** (2015) 20
<http://www.sciencedirect.com/science/article/pii/S0168900214015599>
- [24] Atchison F *et al.* *Phys. Lett.* **B 642** (2006) 24
<http://www.sciencedirect.com/science/article/pii/S037026930601166X>